PHYSICAL REVIEW MATERIALS **8**, 036201 (2024)

Editors' Suggestion

Optical tuning of the diamond Fermi level measured by correlated scanning probe microscopy and quantum defect spectroscopy

Christian Pederson[1,*] Rajiv Giridharagopal,[2] Fang Zhao,[3] Scott T. Dunham,[4]
Yevgeny Raitses,[5] David S. Ginger[2,6] and Kai-Mei C. Fu[1,4,6]

[1]*Department of Physics, University of Washington, Seattle, Washington, 98105, USA*
[2]*Department of Chemistry,University of Washington, Seattle, Washington, 98105, USA*
[3]*Department of Physics, Princeton University, Princeton, New Jersey, 08544, USA*
[4]*Department of Electrical and Computer Engineering, University of Washington, Seattle, Washington, 98105, USA*
[5]*Princeton Plasma Physics Laboratory, Princeton University, P.O. Box 451, Princeton, New Jersey 08543, USA*
[6]*Physical Sciences Division, Pacific Northwest National Laboratory, Richland, Washington 99352, USA*

(Received 29 September 2023; accepted 12 February 2024; published 14 March 2024)

Quantum technologies based on quantum point defects in crystals require control over the defect charge state. Here we tune the charge state of shallow nitrogen-vacancy and silicon-vacancy centers by locally oxidizing a hydrogenated surface with moderate optical excitation and simultaneous spectral monitoring. The loss of conductivity and change in work function due to oxidation are measured in atmosphere using conductive atomic force microscopy and Kelvin probe force microscopy (KPFM). We correlate these scanning probe measurements with optical spectroscopy of the nitrogen-vacancy and silicon-vacancy centers created via implantation 15–25 nm beneath the diamond surface and annealing. The observed charge state of the defects as a function of optical exposure demonstrates that laser oxidation provides a way to precisely tune the Fermi level over a range of at least 2.00 eV. We also observe a significantly larger oxidation rate for implanted surfaces compared to unimplanted surfaces under ambient conditions. Combined with knowledge of the electron affinity of a surface, these results suggest KPFM is a powerful, high-spatial-resolution technique to advance surface Fermi level engineering for charge stabilization of quantum defects.

DOI: 10.1103/PhysRevMaterials.8.036201

I. INTRODUCTION

Quantum point defects in wide band gap semiconductors are utilized for quantum sensing and quantum information applications due to their long spin coherence times and spin-selective optical transitions [1,2]. For a given application, a particular charge state of the defect is required. This charge state can be passively controlled by Fermi level engineering of the host crystal, typically through bulk impurity doping [3–5]. However, control over the Fermi level can be challenging in wide band gap semiconductors due to limits in dopability [6]. For quantum sensors and integrated quantum photonics, the defect must be close (nm to hundreds of nm) to the surface. This opens up an additional control knob, surface Fermi level engineering. Control over the surface Fermi level can be realized via active techniques such as gating [7,8] or passive techniques such as chemical surface functionalization [9–12]. Control over the surface termination is additionally attractive because it not only affects the defect charge state, it also affects defect spin [13] and optical properties [14]. This surface sensitivity indicates a pressing need for engineering atomically ordered surfaces with the desired electronic structure.

A large body of existing work in diamond surface science has focused on electronic applications [15]. Now, the impact of these surfaces on quantum point defect properties in diamond is receiving attention. Optical measurements have directly linked the ratio of fluorescence of near-surface neutral nitrogen-vacancy centers NV^0 and negatively charged NV^- centers to the degree of oxidation and hydrogenation [9,10]. Later work has shown similar switching between the neutral silicon vacancy SiV^0 and negatively charged SiV^- [11]. In both cases, the surface termination was switched in a binary fashion between an oxidized surface and hydrogenated surface. However, a desired defect may require an intermediate termination. For example, in the case of SiV^0, theoretical calculations of the formation energies suggest that near-surface SiV may not be in the desired neutral charge state for strongly hydrogenated or strongly oxidized surfaces [16].

To date, the primary method for determining the effectiveness of the surface treatment is typically the direct optical probing of the quantum defects, in particular when the device size is small (μm) [8] compared to standard large-area surface characterization techniques such as ultraviolet photoelectron spectroscopy (mm). In this work, we combine optical probing with conductive atomic force microscopy (C-AFM) and Kelvin probe force microscopy (KPFM) techniques. The scanning probe techniques work under ambient conditions, high vacuum, on fabricated electronic devices, and even under optical excitation, enabling measurements under practical

---

[*] cpederso@uw.edu.

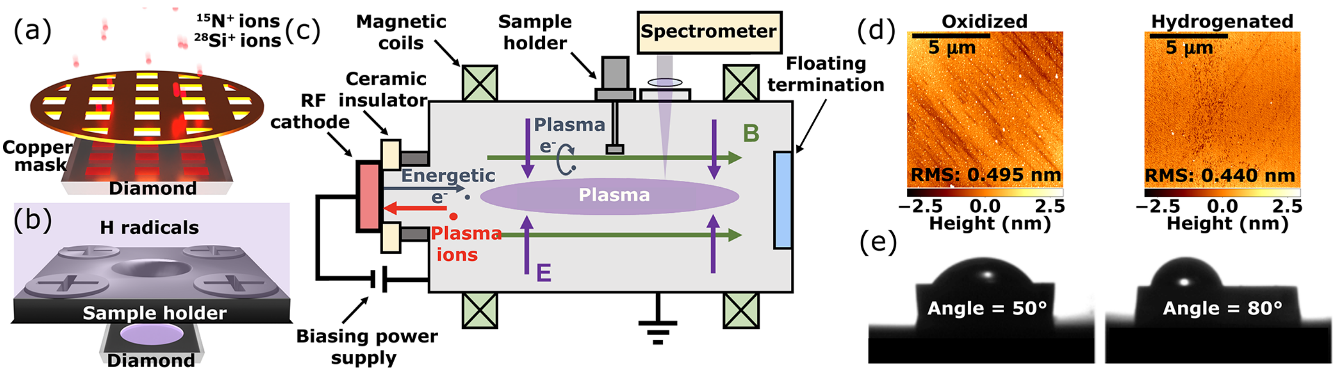

FIG. 1. (a) Schematic of implantation geometry. The diamond substrate is implanted through a TEM grid resulting in squares of implanted nitrogen and silicon. The squares are 28 µm (90 µm) wide in sample A (B). (b) Schematic of the sample holder used in the plasma reactor. A large circular window on the diamond surface is exposed to the hydrogen radicals, while the edges are masked (c) Schematic of cold plasma reactor. (d) AFM topography measurements before and after the hydrogenation showing similar surface roughness. (e) Water wetting angle measurements before and after hydrogenation show the expected increase in hydrophobicity.

experimental conditions. We find a strong correlation between the scanning probe measurements and the charge state and emission intensity of the quantum defects. We further utilize the method to study laser-assisted oxidation, which provides controlled surface modification with optical spatial resolution. Finally, correlated measurements show a significant acceleration of oxidation of hydrogen-passivated surfaces in ambient conditions in the presence of implantation damage.

II. SAMPLE PREPARATION AND ANALYSIS TECHNIQUES

We implanted two chemical vapor deposition diamond substrates on the (100) surface (Element Six, ELSC grade), named A and B, with silicon and nitrogen. The nominal nitrogen and boron substrate concentrations are specified as less than 5 ppb and 1 ppb, respectively. Prior to implantation, we etched the top 5 µm of the surface in an Ar/Cl RIE plasma and oxygen plasma [14] to remove surface damage from polishing and prior implantation. We co-implant both samples with nitrogen and silicon at fluences of 10^{10} cm^{-2} and 10^{11} cm^{-2}, respectively. Sample A (B) has a N$^+$ and Si$^+$ acceleration energy of 10 keV and 19 keV (18 keV and 34 keV), respectively. We implanted at an angle of 7 degrees from normal through a TEM mask, resulting in implantation squares [Fig. 1(a)]. The mean implantation depth for both impurities is 15 nm in sample A and 25 nm in sample B, as simulated by SRIM [17]. We chose the implantation depth such that the quantum defects lie in the band bending region of the surface, and thus are sensitive to surface terminations [9]. We utilized the implanted nitrogen to form NV centers, whose charge state is very sensitive to band bending and relatively well understood, whereas we used silicon for forming SiV in order to further our understanding of SiV charge state stabilization. We annealed sample A (B) at 800 °C (1200 °C) for 2 h under vacuum (10^{-7} mbar) to mobilize the vacancies produced by ion implantation and form both NV and SiV centers, and to anneal out residual implantation damage. Following the vacuum anneal, we boiled the sample in a 1:1:1 mixture of sulfuric, nitric and perchloric acid for 1 h and subsequently annealed at ambient pressure in oxygen at 465 °C for 4 h to form a starting oxidized surface [10].

Next, we exposed the sample surface to a cold hydrogen plasma treatment, which was developed to achieve record hydrogen termination on graphene [18]. We mounted the sample in a holder, which exposes a circular region of the sample to the hydrogen plasma, with the sample edges masked [Fig. 1(b)]. In conventional direct-current (dc) and radio-frequency (rf) plasma processing reactors, high-energy hydrogen ions generated at the plasma-substrate interface (so-called sheath) and energetic atoms generated due to charge-exchange collisions between ions and atoms can induce substantial damage by irreversible etching and sputtering. In contrast, the cold hydrogen plasma is generated by nonthermal electrons in crossed electric and magnetic fields, so-called cross-field or ExB plasma discharge [Fig. 1(c)]. The sample is held beneath the confined plasma to expose the surface to hydrogen radicals (rather than ions). The electric field is directed inward, i.e., away from the substrate, preventing energetic ions from impinging on the substrate. AFM measurements confirm a similar RMS roughness before and after H treatment [RMS = Fig. 1(d)]. Additionally, the sample surface becomes hydrophobic [Fig. 1(e)], which is expected for hydrogen passivation [15]. As we see further below, this masking allows us to probe the continuous region between the oxidized and hydrogenated surfaces.

We performed confocal photoluminescence imaging and spectroscopy at STP to monitor the luminescence from the NV^0, NV$^-$, and SiV$^-$. We excited and oxidized the samples with a 532-nm laser focused to a 500-nm diameter spot. The ratio of the NV$^-$ to NV^0 luminescence is used to serve as a proxy for the Fermi level [9].

For KPFM and C-AFM measurements, we patterned the ground electrode onto the face of the diamond using e-beam evaporation through a shadow mask, and then wire bonded the electrode to a chip carrier. The electrode consists of a 140-nm-thick gold layer deposited on a 10-nm-thick titanium adhesion layer. This lateral geometry allows both KPFM measurements and C-AFM measurements on the same area; the use of a backing plane electrode on a thick insulating substrate would prevent C-AFM measurements. We performed KPFM

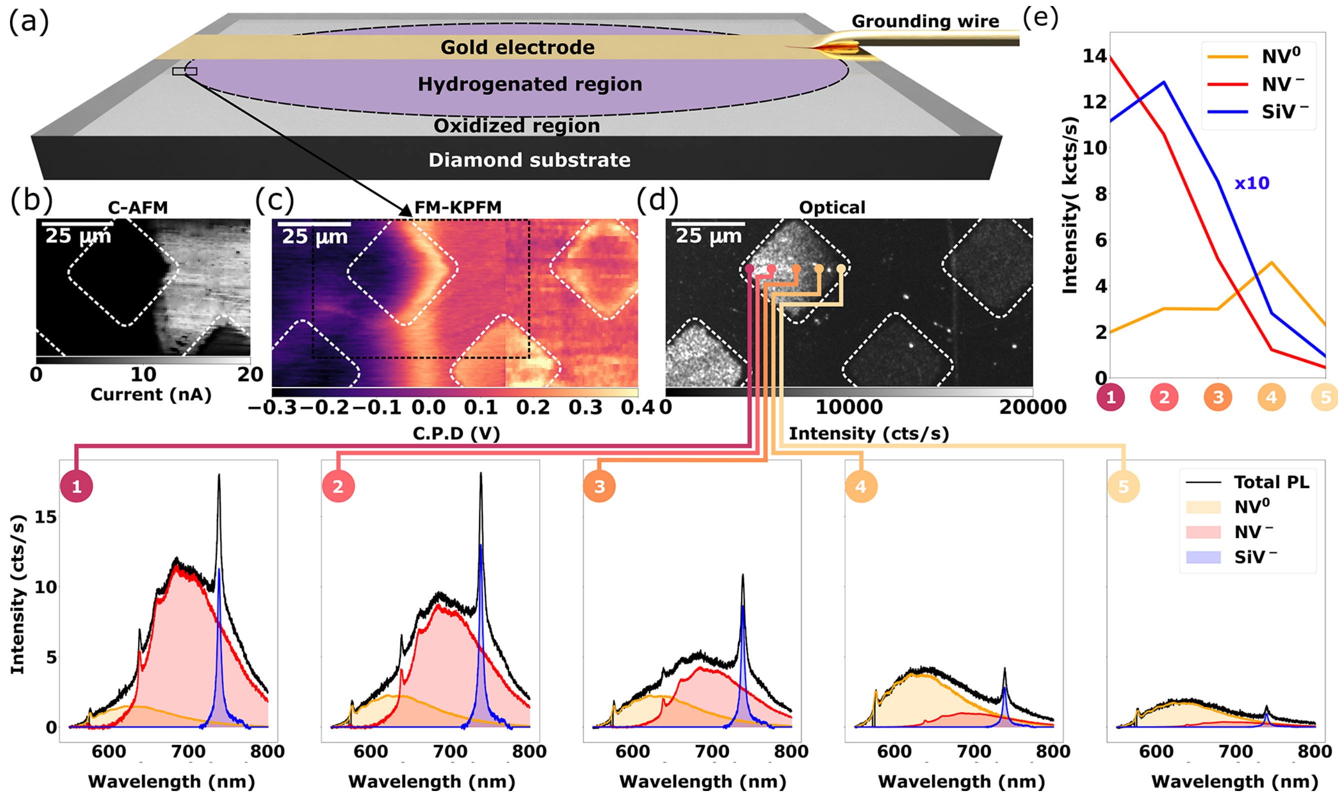

FIG. 2. (a) Schematic of sample with electrode. (b) C-AFM image of sample A (15-nm depth) with a 5-V sample bias. (c) Stitched FM-KPFM image of sample A taken with a 10-nm lift height. A constant −70-mV offset is applied to the right scan to match the CPD in the overlapping region. (d) Confocal photoluminescence image of sample A obtained using 1 mW of 532-nm excitation. Spectra taken at five locations across the boundary are shown below using 0.8 mW at 532 nm. (e) Total PL intensity for the three defect charge states for the spots indicated in (d).

using both amplitude-modulated (AM-KPFM) and frequency-modulated (FM-KPFM) methods. FM-KPFM is sensitive to the electrostatic force gradient, rather than the electrostatic force as in AM-KPFM, and therefore yields better spatial resolution and a more accurate contact potential difference (CPD), the difference between the work function of the sample and the tip. AM-KPFM is more efficient at scanning large areas quickly [19]. The absolute value of the contact potential difference measured in the KPFM signal is dependent upon the material and geometry of the tip. We performed all AFM measurements with an MFP3D AFM (Oxford Instruments) using metal-coated cantilevers (KPFM: BudgetSensors ElectriTap190-G cantilevers; C-AFM: BudgetSensors CONTG-B contact-mode cantilevers). We performed FM-KPFM using custom, publicly available code [20] written in IGOR PRO, as in previous work [21]. We used a typical lift height of 10 nm during KPFM acquisition.

III. CORRELATED PL, KPFM, AND C-AFM IMAGING

We perform correlated C-AFM, KPFM, and PL spectroscopy around a narrow transition region between the oxygen and hydrogen termination transition [Fig. 2(a)]. C-AFM measurements [Fig. 2(b)] confirm that the hydrogen-terminated surface on the right is conductive while the left oxygen-terminated surface is insulating. This provides further verification that the hydrogen termination has pushed the Fermi level into the valence band. Additionally, a dramatic increase in resistance is observed above the implantation squares, suggesting either a loss of hydrogenation in these regions or increased scattering due to interactions between the holes and the residual implantation damage. Further measurements below support the former hypothesis.

FM-KPFM in Fig. 2(c) in the same region shows a 250–320 mV potential increase from the oxidized to hydrogenated surface. The size and sign of the change in surface potential is similar to prior reports, which range between 100–300 mV [22,23]. Similar to the C-AFM data, one of the most striking features of the KPFM image is the ability to visualize the implantation squares. Additionally, we note that the CPD does not monotonically increase from the oxygen-terminated to hydrogen-terminated side, but rather has a maximum between the two regions. This behavior was observed even in the region that has not been implanted and will be discussed further below.

During photoluminescence imaging, we collected a spectral band of 653–815 nm, which includes PL contributions for NV^0, NV^-, and SiV^-. The PL image shown in Fig. 2(d) shows bright PL emission under the oxidized surface, with very low fluorescence shown under the hydrogenated surface. Spatially resolved spectra across the square, which lies on the termination boundary show that not only does the total intensity change (black spectra), but the relative contributions of the three defects, NV^-, NV^0, and SiV^- vary as well. We extracted

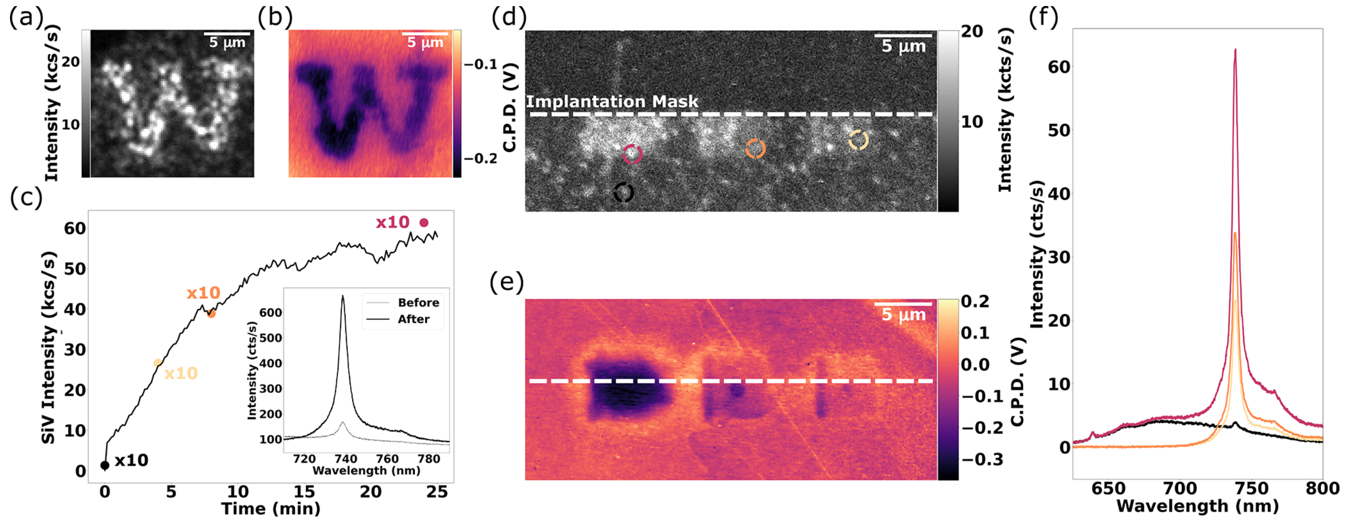

FIG. 3. (a) Confocal PL image of sample A (15 nm) after laser-assisted oxidation. Laser-assisted oxidation is performed with 20 mW (1.0×10^{10} mW/cm^2) of 532 nm, while confocal imaging utilizes 1 mW (5.1×10^8 mW/cm^2) of 532 nm. The entire time of exposure was 10 h. (b) AM-KPFM image of sample A after laser-assisted oxidation. (c) Time dependence of the SiV^- PL intensity on sample B (25 nm) using 30 mW (1.5×10^{10} mW/cm^2) of 532 nm excitation. Colored data points correspond to the SiV^- intensity from the three laser-assisted exposed regions. Inset: Representative PL spectra taken at the start and end of the laser exposure used to determine total PL intensity. (d) Confocal image of three laser-assisted exposed squares on sample B using 1 mW of 532-nm excitation. The dashed white line denotes the implantation square boundary. PL background from deeper native NV is observed throughout the implantation square (bottom half). (e) FM-KPFM image of the laser-assisted oxidized squares on sample B. (f) Photoluminescence spectra corresponding to the four marked regions in (d) and the colored data points in (c) obtained using 1 mW of 532-nm excitation.

these relative contributions by fitting the total spectrum to a weighted sum of the individual defect spectra [Fig. 2(d)]. Figure 2(e) depicts the change in PL intensity for the three defects across the termination. The PL from the negatively charged defects monotonically quench with hydrogenation, while the neutral NV^0 PL increases but eventually quenches at the highest exposure. These results are consistent with prior reports of NV luminescence after hydrogen plasma treatment, which show NV centers can be left in the neutral or even optically dark positively charged NV^+ state [9], dependent on the level of hydrogenation.

IV. OPTICAL CONTROL OVER THE SURFACE FERMI LEVEL

In this section, we utilize KPFM to demonstrate that the hydrogen-terminated surface can be oxidized via laser irradiation in air. Figure 3(a) depicts a confocal image of a hydrogen-terminated region in sample A. Prior to imaging, we patterned a W on an implantation square using a 20-mW 532-nm laser in air focused to a 500-nm-diameter spot corresponding to an irradiance of $1.0 \times 10^{10}\mathrm{mW/cm^2}$. The laser-exposed implantation square is visibly brighter, similar to the oxygen-terminated surface. AM-KPFM of the same region [Fig. 3(b)] reveals that the bright PL corresponds to a decrease in the work function. In AM-KPFM, due to contributions of the work function far from the sharp tip, this value likely represents a lower limit for the shift. These correlated measurements suggest that the level of hydrogen termination and thus the surface Fermi level can be tuned with laser irradiation. This result is consistent with the observation of diamond etching via laser-induced local oxidation, which has been reported at much higher laser powers [24]. At the laser intensities used in this work, no etching is detectable via atomic-force microscopy. Finally we observe that the NV center responds to the laser-assisted oxidation as expected, showing a conversion to the desired negatively charged state, which is shown in Sec. I of the Supplemental Material [25].

We tested the hypothesis that the oxidation can be continuously tuned using sample B. Figure 3(c) shows a time trace of the PL intensity from SiV^- at a single excitation spot plotted under 30 mW (1.5×10^{10} mW/cm^2) excitation. The increase in intensity is observed to saturate after around 15 min. This relatively slow process and the optical spatial resolution enable very precise control over the Fermi level. In contrast to sample A, the spectra taken on sample B after exposure show that SiV and not NV contribute to the majority of the signal. The lower formation yield of sample B NV centers is attributed to the higher annealing temperature [31].

We then exposed three $5x5$ µm squares using the 30 mW (1.5×10^{10} mW/cm^2) excitation, varying the exposure time to obtain three different oxidation levels. These squares overlap the edge of an implantation square, allowing us to study differences in the changes in PL and surface potential between implanted and nonimplanted regions. As expected, the PL intensity only increases in the part of the square over the implanted defects [Fig. 3(d)], while the entire exposed square is modified in the KPFM image [Fig. 3(e)]. The nonlinear response in the SiV^- PL intensity with laser exposure is used to estimate the exposure from the tuning curve [Fig. 3(c)]. Similar to the W, we observe an increase in PL intensity and a decrease in surface potential. Spectra in Fig. 3(f) on the exposed squares confirm that the PL enhancement is coming from the SiV^-.

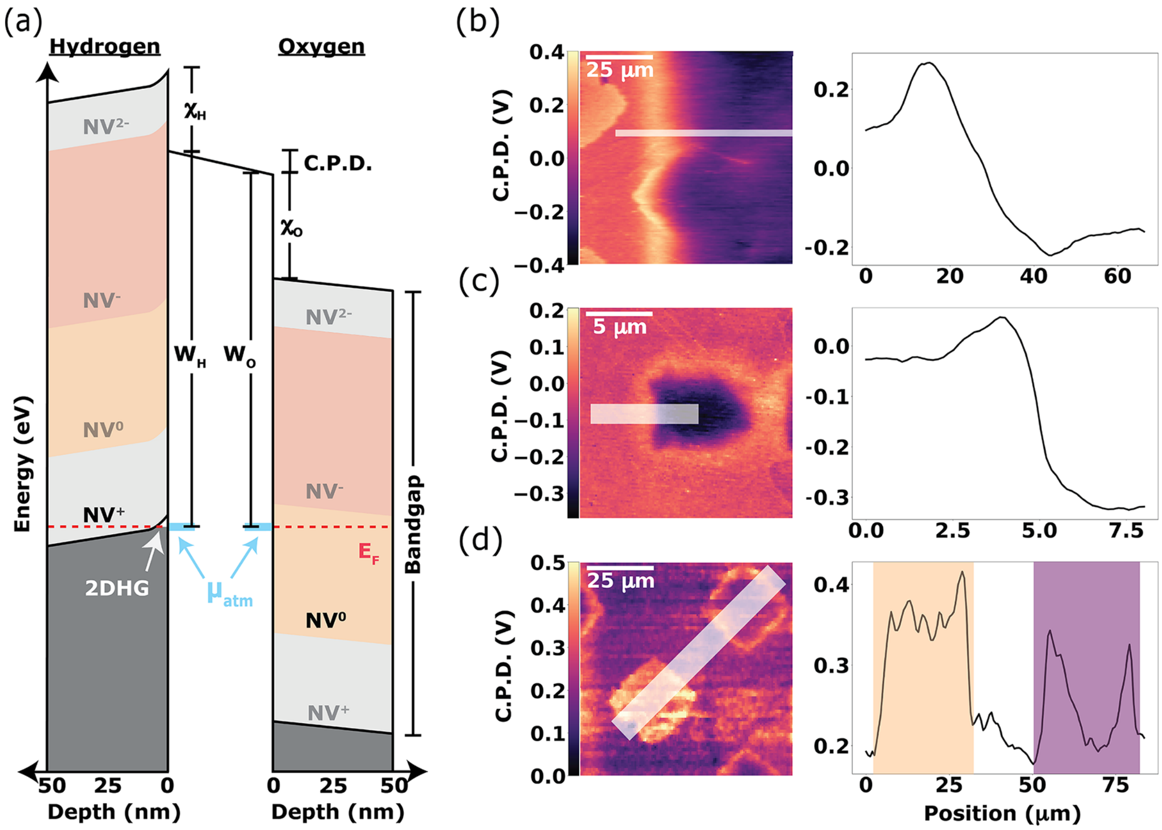

FIG. 4. (a) Band diagram of the top 50 nm of hydrogenated and oxidized diamond surfaces using formation energies calculated in Ref. [30]. The Fermi level for hydrogenated diamond is located at approximately the valence band maximum where the 2D hole gas (2DHG) forms. The oxidized surface is shown pinned 2.4 eV above the valence band due to the presence of surface defects. (b) Left: FM-KPFM image depicting the boundary between the masked oxidized and hydrogenated diamond surface of sample A (15 nm). Right: Line scan across the unimplanted region, averaged over 2.5 μm. (c) Left: FM-KPFM image depicting the square created by the longest exposure to the laser on sample B (25 nm). Right: FM-KPFM line scan across the square's boundary, averaged over 1.5 μm. (d) Left: FM-KPFM image of two implantation squares of sample A after hydrogen passivation. Right: Line scan across the two implantation squares, averaged over 10 μm. The implantation squares are indicated by the shaded regions.

V. DISCUSSION AND OUTLOOK

In these experiments, KPFM and C-AFM, correlated with photoluminescence measurements, enable us to link the brightening of quantum defect luminescence to surface properties. This connection can be understood using the band bending diagram depicted in Fig. 4(a). Under both oxidized and hydrogenated nitrogen-doped diamond, electron transfer from nitrogen donors to surface acceptors results in an upward band bending. This upward band bending is more obvious over larger depths than the 50 nm depth shown in Fig. 4(a) and can be seen in Sec. II of our Supplemental Material [25]. In the case of hydrogenated diamond, there is an additional upward bending contribution from the transfer of electrons in the valence band to atmospheric acceptors on the surface. This surface transfer doping mechanism results in the conductive two-dimensional (2D) hole gas [15] detected by C-AFM. It is also responsible for the pinning of the Fermi level near the valence band maximum. Under oxidized diamond, the electrons from the nitrogen donors are trapped at surface defects [27] pinning the Fermi level midgap. The charge state of the near-surface defects can be determined from the Fermi level through the calculation of formation energies. In Fig. 4(a) we illustrate the possible charge states of the NV center as shaded regions within the band gap. The region that contains the Fermi level is the equilibrium state, thus for hydrogenated diamond, we expect the NV^+ state. In oxidized diamond, the charge state will depend on the density of the trap states and will lie within the NV^0 and NV^- bands [27].

Also depicted in Fig. 4(a) is the difference in CPD between the two surfaces. Both the Fermi level and electron affinity will change with surface termination, which can result in a seemingly complex spatial dependence of the CPD. In Fig. 4(b), a horizontal line scan of the work function is shown across the hydrogenated-oxidized boundary. For simplicity, this scan is taken in a region with no implantation. An initial increase in the work function is observed as the diamond becomes oxidized, before finally dropping 250–320 meV below the hydrogenated level. This behavior can be understood by noting that the CPD has two contributions, the electron affinity χ_e and the Fermi level E_F. Specifically, the change in CPD over a material with a constant band gap is given by $\Delta W = \Delta\chi_e - \Delta E_F$, where W is the work function, χ_e is the electron affinity, and E_F is the Fermi level measured from the valence band maximum. The electron affinity should monotonically increase as oxygen replaces hydrogen due to the opposite polarity of the two surface dipole moments. This increase can happen spatially across the surface due to masking, or over time by our laser-induced oxidation. The Fermi level also increases as the surface is oxidized; on a hydrogenated surface, it can lie as deep as 0.7 eV below the valence band [32], while oxidized diamond is believed to be pinned around 1.8–2.4 eV [27,28] above the valence band. We utilize the upper estimate 2.4 eV for the oxidized Fermi level to explain our measurements, which is discussed in Sec. II of the Supplemental Material [25]. The dependence of the Fermi level on the surface termination is more complicated than the electron affinity dependence as it also depends on electron transfer between the diamond and the surface wetting layer. We hypothesize that the initial increase in the work function is caused by a Fermi level that remains pinned near the valence band despite the increasing electron affinity.

The nonmonotonic behavior of the CPD with oxidation results in some unique features in the KPFM images of laser-exposed and defect-implanted surfaces. In Fig. 4(c) a KPFM scan of the square with the largest laser exposure is shown. We observe a dark oxidized patch surrounded by a lighter halo. The work function of this halo is even higher than the surrounding unexposed surface. We attribute this halo to the Gaussian laser profile, which results in a weaker exposure at the edge of the square, combined with the CPD's nonmonotonic dependence with oxidation. This effect is analogous to the boundary effect we observed in Fig. 4(b).

The nonmonotonic CPD effect can also be used to explain two different characteristic behaviors observed at the surface of seemingly identical implantation squares. These squares have not received the laser oxidation treatment. As illustrated in Fig. 4(d), we observe an increase in work function over the entire surface of some squares, while others we observe only an increase in a halo around the square. For the halo squares, the interior may exhibit a slightly higher to significantly lower work function than outside the square. These results can be explained by accelerated oxidation of the diamond surface in ambient conditions due to implantation damage, even at the low implantation fluence in this study corresponding to one ion per (30 nm)^2. Squares that are early in the oxidation process will have an all-positive surface, with the halo forming later in the process when the interior of the square becomes more oxidized. This implantation-induced acceleration is significant; only the implanted regions in sample A show signs of oxidation after two years in ambient conditions. More theoretical work is needed to elucidate the mechanism for accelerated oxidation given the importance of near-surface defects for quantum technologies.

In summary, we utilize correlated scanning-probe microscopy and photoluminescence to study surface oxidation of hydrogenated diamond surfaces. We continuously vary the hydrogenation/oxidation in two ways: by shadow masking an oxygen-terminated surface in a cold hydrogen plasma and by controlled laser-assisted oxidation. In both cases, we observe the nonmonotonic increase in work function with oxidation. KPFM measurements are consistent with the observed charge state of quantum defects beneath these functionalized surfaces. Correlated measurements further uncover that the surfaces over implanted defects oxidize more quickly than pristine surfaces. Combined with knowledge of the electron affinity of a surface, these results indicate KPFM can be a powerful, high-spatial-resolution technique to advance surface Fermi level engineering for charge stabilization of quantum defects.

ACKNOWLEDGMENTS

The initial collaborative work for this proposal was supported by the NSF through the University of Washington Materials Research Science and Engineering Center, DMR-1719797, DMR-2308979. K.M.C.F. and C.P. were partially supported by DOE Office of Science Award No. DE-SC0022210. D.S.G. and R.G. acknowledge the U.S. Department of Energy ESPM (DOE-SC0013957) for supporting the scanning probe microscopy work. Plasma treatment was supported by Princeton Collaborative Research Facility (PCrf) and funded by the U.S. Department of Energy (DOE), Office of Fusion Energy Sciences under Contract No. DE-AC02-09CH11466. Device fabrication was performed at the Washington Nanofabrication Facility/Molecular Analysis Facility, a National Nanotechnology Coordinated Infrastructure (NNCI) site at the University of Washington with partial support from the National Science Foundation via Awards No. NNCI-1542101 and No. NNCI-2025489. We thank Nathalie de Leon for helpful discussions and Zihuai Zhang and Sounak Mukherjee for confirmation of the SiV charge state measurement.

---

[1] G. Wolfowicz, F. J. Heremans, C. P. Anderson, S. Kanai, H. Seo, A. Gali, G. Galli, and D. D. Awschalom, Nature Rev. Mater. **6**, 906 (2021).

[2] L. C. Bassett, A. Alkauskas, A. L. Exarhos, and K.-M. C. Fu, Nanophoton. **8**, 1867 (2019).

[3] D. B. Radishev, M. A. Lobaev, S. A. Bogdanov, A. M. Gorbachev, A. L. Vikharev, and M. N. Drozdov, J. Lumin **239**, 118404 (2021).

[4] Y. Doi, T. Fukui, H. Kato, T. Makino, S. Yamasaki, T. Tashima, H. Morishita, S. Miwa, F. Jelezko, Y. Suzuki, and N. Mizuochi, Phys. Rev. B **93**, 081203(R) (2016).

[5] B. C. Rose, D. Huang, Z.-H. Zhang, P. Stevenson, A. M. Tyryshkin, S. Sangtawesin, S. Srinivasan, L. Loudin, M. L. Markham, A. M. Edmonds, D. J. Twitchen, S. A. Lyon, and N. P. de Leon, Science **361**, 60 (2018).

[6] W. Walukiewicz, Appl. Phys. Lett. **54**, 2094 (1989).

[7] S. Karaveli, O. Gaathon, A. Wolcott, R. Sakakibara, O. A. Shemesh, D. S. Peterka, E. S. Boyden, J. S. Owen, R. Yuste, and D. Englund, Proc. Natl. Acad. Sci. USA **113**, 3938 (2016).

[8] C. Schreyvogel, V. Polyakov, R. Wunderlich, J. Meijer, and C. E. Nebel, Sci. Rep. **5**, 12160 (2015).

[9] M. V. Hauf, B. Grotz, B. Naydenov, M. Dankerl, S. Pezzagna, J. Meijer, F. Jelezko, J. Wrachtrup, M. Stutzmann, F. Reinhard, and J. A. Garrido, Phys. Rev. B **83**, 081304(R) (2011).

[10] K.-M. C. Fu, C. Santori, P. E. Barclay, and R. G. Beausoleil, Appl. Phys. Lett. **96**, 121907 (2010).

[11] Z.-H. Zhang, J. A. Zuber, L. V. H. Rodgers, X. Gui, P. Stevenson, M. Li, M. Batzer, Marcel.li Grimau Puigibert, B. J. Shields, A. M. Edmonds, N. Palmer, M. L. Markham, R. J. Cava, P. Maletinsky, and N. P. de Leon, Phys. Rev. Lett. **130**, 166902 (2023).

[12] L. V. H. Rodgers, S. T. Nguyen, J. H. Cox, K. Zervas, Z. Yuan, S. Sangtawesin, A. Stacey, C. Jaye, C. Weiland, A. Pershin, A. Gali, L. Thomsen, S. A. Meynell, L. B. Hughes, A. C. B. Jayich, X. Gui, R. J. Cava, R. R. Knowles, and N. P. de Leon (unpublished).

[13] S. Sangtawesin, B. L. Dwyer, S. Srinivasan, J. J. Allred, L. V. H. Rodgers, K. De Greve, A. Stacey, N. Dontschuk, K. M. O'Donnell, D. Hu, D. A. Evans, C. Jaye, D. A. Fischer, M. L. Markham, D. J. Twitchen, H. Park, M. D. Lukin, and N. P. de Leon, Phys. Rev. X **9**, 031052 (2019).

[14] S. Chakravarthi, C. Pederson, Z. Kazi, A. Ivanov, and Kai-Mei C. Fu, Phys. Rev. B **104**, 085425 (2021).

[15] K. G. Crawford, I. Maini, D. A. Macdonald, and D. A. Moran, Prog. Surf. Sci. **96**, 100613 (2021).

[16] A. Gali and J. R. Maze, Phys. Rev. B **88**, 235205 (2013).

[17] J. F. Ziegler, M. Ziegler, and J. Biersack, Nucl. Instrum. Methods Phys. Res., Sect. B **268**, 1818 (2010).

[18] F. Zhao, Y. Raitses, X. Yang, A. Tan, and C. G. Tully, Carbon **177**, 244 (2021).

[19] W. Melitz, J. Shen, A. C. Kummel, and S. Lee, Surf. Sci. Rep. **66**, 1 (2011).

[20] Code available at https://github.com/GingerLabUW/AFMSoftware.

[21] J. Yu, R. Giridharagopal, Y. Li, K. Xie, J. Li, T. Cao, X. Xu, and D. S. Ginger, Nano Lett. **21**, 3280 (2021).

[22] M. Tachiki, Y. Kaibara, Y. Sumikawa, M. Shigeno, H. Kanazawa, T. Banno, K. Soup Song, H. Umezawa, and H. Kawarada, Surf. Sci. **581**, 207 (2005).

[23] B. Rezek and C. Nebel, Diam. Relat. Mater. **14**, 466 (2005).

[24] V. Ral'chenko, K. Korotushenko, A. Smolin, and E. Loubnin, Diam. Relat. Mater. **4**, 893 (1995).

[25] See Supplemental Material at http://link.aps.org/supplemental/10.1103/PhysRevMaterials.8.036201 for characterization of NV centers before and after laser treatment and a detailed discussion of band bending, which includes Refs. [26–30].

[26] R. Farrer, Solid State Commun. **7**, 685 (1969).

[27] A. Stacey, N. Dontschuk, J.-P. Chou, D. A. Broadway, A. K. Schenk, M. J. Sear, J.-P. Tetienne, A. Hoffman, S. Prawer, C. I. Pakes, A. Tadich, N. P. de Leon, A. Gali, and L. C. L. Hollenberg, Adv. Mater. Inter. **6**, 1801449 (2019).

[28] Y. Itoh, Y. Sumikawa, H. Umezawa, and H. Kawarada, Appl. Phys. Lett. **89**, 203503 (2006).

[29] W. Mönch, *Semiconductor Surfaces and Interfaces*, Springer series in surface sciences (Springer, Berlin, 1995).

[30] P. Deák, B. Aradi, M. Kaviani, T. Frauenheim, and A. Gali, Phys. Rev. B **89**, 075203 (2014).

[31] J. O. Orwa, C. Santori, K. M. C. Fu, B. Gibson, D. Simpson, I. Aharonovich, A. Stacey, A. Cimmino, P. Balog, M. Markham, D. Twitchen, A. D. Greentree, R. G. Beausoleil, and S. Prawer, J. Appl. Phys. **109**, 083530 (2011).

[32] B. Rezek, C. Sauerer, C. Nebel, M. Stutzmann, J. Ristein, L. Ley, E. Snidero, and P. Bergonzo, Appl. Phys. Lett. **82** (2003).